Appl. Phys. B 65, 175–188 (1997)

Applied Physics B Lasers and Optics

© Springer-Verlag 1997

Invited paper

All-solid-state cavity-dumped sub-5-fs laser

A. Baltuška[1], Z. Wei[1,*], M.S. Pshenichnikov[1], D.A. Wiersma[1], Róbert Szipőcs[2]

[1] Ultrafast Laser and Spectroscopy Laboratory, Department of Chemistry, University of Groningen, Nijenborgh 4, 9747 AG Groningen, The Netherlands (Fax: +31-50-3634441, E-mail: D.A.Wiersma@chem.rug.nl)
[2] Research Institute for Solid State Physics, P.O. Box 49, H-1525 Budapest, Hungary (E-mail: rsz@power.szfki.kfki.hu)

Received: 19 March 1997/Revised version: 9 May 1997

Abstract. We discuss in detail a compact all-solid-state laser delivering sub-5-fs, 2-MW pulses at repetition rates up to 1 MHz. The shortest pulse generated thus far measures only 4.6 fs. The laser system employed is based on a cavity-dumped Ti:sapphire oscillator whose output is chirped in a single-mode fiber. The resulting white-light continuum is compressed in a novel high-throughput prism chirped-mirror Gires–Tournois interferometer pulse compressor. The temporal and spectral phase of the sub-5-fs pulses are deduced from the collinear fringe-resolved autocorrelation and optical spectrum. The derived pulse shape agrees well with the one retrieved from the measured group delay of the continuum and calculated characteristics of the pulse compressor.

PACS: 42.65.Re; 42.30.Rx; 42.81.-I

Ever since pulsed lasers were invented there has been a race towards shorter optical pulses [1]. Next to the fact that the breaking of any record is a challenge, a major scientific driving force came from dynamical studies showing that ultrashort pulses were essential to the exploration of elementary processes in chemistry, photobiology, and physics. For instance, the primary step in bond-breaking reactions (femtochemistry) [2], the rate of electron-transfer in photosynthetic reaction centra [3, 4], and the time scales of relaxation processes in condensed phase [5, 6] could only be time-resolved with femtosecond excitation pulses. On the road towards femtoseconds pulse generation a better grasp of the underlying physics proved to be essential. A milestone here was the development of the colliding pulse modelocked (CPM) laser [7]. When the importance of a careful balance between the group delay and dispersion on pulse formation was recognized [8, 9], sub-100-fs optical pulses became feasible [10, 11]. Further development ultimately led to the prism-controlled CPM laser [12, 13], which delivered pulses of ~ 30 fs. It was this CPM laser that laid the foundation for many ground-breaking experiments in the past decade, from the observation of wave-packet motion in chemical reactions [14] to the exploration of carrier dynamics in semiconductors [15, 16].

Another crucial invention for ultrashort optical pulse generation was the technique of fiber pulse compression [17]. A relatively long pulse is injected into a single-mode fiber and via the combined action of self-phase-modulation [18] and dispersion becomes spectrally broadened, carrying an almost linear chirp [19]. This spectrally and temporally broadened pulse is subsequently compressed by a pair of gratings [20–22], prisms [10, 23], or their combination [24, 25] to a much shorter pulse. The compressor's action is to retard in a well-defined manner the frequencies of the pulse that have advanced. Pulse compression of the amplified output of the CPM laser culminated in the generation of optical pulses of 6 fs (assuming a hyperbolic secant pulse profile) in 1987 [25]. The electric field of such a pulse exhibits only 4.5 oscillations at its FWHM.[1] With these ultrashort pulses, photon echoes in solution could be studied for the first time [26–28], and their large spectral widths turned out to be very useful for pump–probe experiments in photobiology [29, 30].

A new era in ultrafast laser technology began with the development of the fs modelocked Ti:sapphire laser [31], which routinely generates pulses of about 10-15 fs [32–37]. In addition, this laser exhibits low amplitude noise and is extremely reliable. Not surprisingly, in the past five years Ti:sapphire-based lasers have replaced the CPM lasers in many laboratories as new ultrafast light sources. Sub-10-fs pulse formation from a Ti:sapphire laser also looked promising, as the fluorescence bandwidth of the lasing material [38] allows for pulses as short as 4 fs. However, despite much work, the shortest pulses generated by this laser to date are $\sim$ 7-8 fs in duration [39–44] and according to current understanding this seems to be the practical limit [42, 45, 46].

With the development of a 13-fs cavity-dumped laser, pulse compression was shown to be a viable route towards

*Present address: Institute of Physics, Chinese Academy of Science, Beijing 100080, P.R. of China

[1] The frequently cited number of 3 oscillations [6, 25] refers to the duration of the intensity envelope, which, in contrast to the electric field, contains no oscillations at the optical frequency.

pulses of less than 6 fs [47]. Another very promising development was the use of a hollow fiber for spectral broadening of ultrashort pulses [48]. A distinct advantage of a hollow fiber is that it can stand high intensities, allowing pulses of mJ energy to be compressed.

Recently we showed that pulse compression of the output of a cavity-dumped Ti:sapphire laser can produce pulses of about 5 fs at repetition rates of up to 1 MHz [49, 50]. The shortest pulses were attained by using a prism-grating compressor; slightly longer pulses were obtained from the higher-throughput prism-chirped mirror compressor. It was also suggested that with custom-designed chirped mirrors, shorter pulses with higher pulse energies should be possible. Nisoli et al. recently showed that by using a hollow fiber, $\sim$ 20-μJ, sub-5-fs pulses can be generated at a 1-kHz repetition rate [51].

In this paper we report on the generation of sub-5-fs pulses from a cavity-dumped Ti:sapphire laser using a prism chirped mirror Gires–Tournois interferometer compressor. Group delay measurements of the generated continuum, which served as input for the design of this novel compressor, are discussed. It is shown that the pulse shape and spectral phase can be determined from the collinear autocorrelation function in combination with the optical spectrum. A similar pulse shape is calculated when the optical spectrum and phase difference between the pulse compressor and continuum are used as input.

Precise knowledge of the amplitude and phase of ultrashort pulses is extremely important in many experiments, especially when dynamics occur on the time scale of the pulse width. An example is femtosecond photon echo in solution, where explicit use of the pulse shape in calculations of the echo relaxation moved essential [52, 53]. Another example is coherent control of wave-packet motion and bond-breaking reactions [54–56]. More generally, a detailed description of the molecule–light-field interaction requires full knowledge of the electric field. The applicability of the so-called slowly varying envelope approximation in experiments with ultrashort pulses becomes questionable [57]. In fact this approximation may break down and in that case new effects are to be expected.

In Sect. 1 we discuss the cavity-dumped laser used to produce the pulses that generate the continuum to be compressed. In Sect. 2 the spectral phase of the continuum is discussed, and in Sect. 3 the temporal shape of the continuum is dealt with and compared to calculations based on spectral phase measurements. In Sect. 4 the spectral and temporal shape of the continuum are commented on. Sect. 5 deals with the compressor and Sect. 6 discusses the pulse–duration measurements. In Sect. 7 we demonstrate how the amplitude and phase of the compressed pulse can be reconstructed from measurement of the interferometric autocorrelation and the spectrum of the pulse. Sect. 8 provides a summary and suggests some applications of this compact sub-5-fs, 2-MW laser.

1 Cavity-dumped Ti:sapphire laser and white-light continuum generation

Figure 1 displays the schematic of the self-mode-locked cavity-dumped Ti:sapphire laser used for continuum generation. It represents the next version of a design reported earlier [47]. Compared to the conventional Ti:sapphire oscillator [32, 36, 58], its cavity-dumped counterpart incorporates an additional mirror fold around an acousto-optic modulator [59]. In this way the intracavity pulse energy is stored in a relatively high-Q cavity, which can be switched out of the resonator at any desired repetition rate. The maximal pulse energy of a cavity-dumped Ti:sapphire laser is typically a factor of 10 higher than that from its non-cavity-dumped counterpart. A careful cavity design ensures that the Kerr-lens self-mode-locking action is not disturbed by the extra fold and by the added dispersion due to the Bragg cell. The best performance of the system is achieved when the fold mirrors of the cavity dumper are separated by nearly a confocal distance and the mirror fold around the Ti:sapphire crystal set to the inner edge of the second stability zone [47]. This configuration allows the system to operate under soft-aperture Kerr-lens mode-locking conditions, thus making the oscillator less sensitive to perturbations caused by the cavity-dumping process and mechanical instabilities [47, 60–62] than in the first stability zone. In the last case the hard aperture needed to initiate the mode-locking reduces the intracavity power.

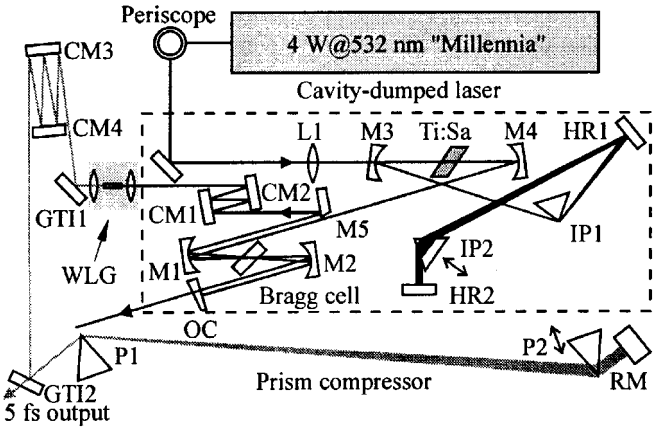

Fig. 1. Schematic of an all-solid-state sub-5-fs laser. Ti:Sa 4-mm-long Ti:Sapphire crystal (Union Carbide); L1 $f = 12.5$-cm lens; M1–M4 $r = -10$-cm cavity mirrors; HR1, HR2 high reflectors (CVI); OC $T = 2\%$ output coupler (CVI); M5 pick-off mirror (Newport BD2); IP1, IP2 intracavity 69° fused-silica prisms; CM1, CM2 chirped mirrors for pre-compression (R&D Lezer Optika); WLG white-light generator; GTI1, GTI2 Gires-Tournois interferometers (R&D Lezer Optika); CM3, CM4 chirped mirrors for pulse compression (R&D Lezer Optika); P1, P2 45° fused-silica prisms; RM low-dispersion overcoated silver roof mirror (R&D Lezer Optika). The cavity-dump beam, in reality ejected in the vertical plane, is depicted here as being displaced in the horizontal plane. The compressor output beam passes just above GTI2. The solid arrow through the OC shows the 82-MHz output used in cross-correlation experiments. The whole set-up occupies a work space of 1 m × 1.5 m on an optical table

Compared to the earlier design [47] the current version of the cavity-dumped Ti:sapphire laser has been significantly improved and presents a more versatile and compact master oscillator. First, the argon-ion pump laser has been replaced by an intracavity-doubled Nd:YVO_4 laser (Spectra Physics Millennia). The superior beam-pointing stability and noise characteristics of this diode-pumped solid-state laser allow the pump power to be reduced to $\sim$ 4 W. Second, by the introduction of a high reflector (HR1) in the prism arm, the cavity has been folded, which led to a more compact laser. Third, the output coupler OC has been placed at the nondispersive end of the cavity, providing an additional output at 82 MHz. Last,

we have saved space by replacing the output (cavity-dumped) pulse pre-compressor, consisting of four prisms [50], with two chirped mirrors [63].

With a 3-mm-thick Bragg cell (Harris), driven by a 5-W electronic driver (CAMAC Systems), the laser dumps ∼ 13-fs, 40-nJ pulses at a 1-MHz repetition rate. Pulses up to 45 nJ are generated when the rf signal is amplified to 16 W by an rf power amplifier (CAMAC Systems). Even higher pulse energies are available at lower repetition rates. Usage of the CAMAC rf driver enhances the contrast ratio between the preceding/trailing and dumped pulses from 1:150 [64] to ∼ 1 : 1000. The last figure is similar to the contrast ratio achieved when using an electro-optical cavity-dumper [65], be it that in the latter case the repetition rate is limited by ∼ 10 kHz.

The pre-compressed 13-fs pulses from the cavity-dumped laser, with 75-nm spectral bandwidth around 790 nm, were launched into a single-mode polarization-preserving fiber (Newport, F-SPV, 2.75-μm core diameter) through a 18/0.35 microscope objective (Melles Griot). The optimal fiber length calculated according to [19] was ∼ 1 mm; however, for practical reasons connected to the mounting of the fiber, we used a piece of ∼ 3.5 mm. Angular alignment of the fiber along the longitudinal axis proved necessary to prevent polarization rotation of the light passing through the fiber as a result of chromatic anisotropy. A 3D piezo-driven (Piezo-Jena) fiber-positioning stage is used to simplify the alignment procedure. To keep the fiber tip dust-free, a constant flow of dry nitrogen was applied to the focusing area. No damage to the fiber was observed for up to 40-nJ pulses. Other types of fibers from different manufacturers were also tested; however, the ability to withstand high input intensities (∼ 10 TW/cm^2) seems a unique property of Newport single-mode fibers. As of now, we have no explanation for this phenomenon.

The fiber output was recollimated by a low-dispersion objective lens (LLU-3-10-LMO, Optics for Research). The white-light continuum, generated by self-phase modulation exhibits approximately a fourfold spectral broadening compared to the initial spectrum (Fig. 2). The optimal pulse energy for injection into the fiber was found to be ∼ 35 nJ, as judged by the quality of the generated continuum. In this case, the pulse energy measured after recollimation of the continuum is about 18 nJ. The long-term stability of the continuum intensity measured at several wavelengths varies from ∼ 0.7% rms at the edges of the spectrum (below 500 nm and above 1100 nm) to less than 0.5% rms near the central frequencies.

The blue-shifted wing of the continuum reaches into the UV, and the red-shifted part stretches into the near infrared, even beyond the spectral cutoff of the silicon detector used for the spectral measurements (Fig. 2). The shortest pulse attainable by compression of this continuum is obtained by Fourier transformation of the spectrum, assuming a constant spectral phase. This yields a pulse duration of ∼ 3.7 fs (Fig. 2, inset). Note that despite the irregular spectrum of the continuum the ideally compressed pulse looks very clean. It is also worth pointing out that the low-intensity wings of the continuum – excluded in the compression scheme to be discussed later – carry enough intensity for a variety of spectroscopic applications. Moreover, use of a long piece of fiber enables delivery of the pulse to a remote point in applications where the spectral bandwidth rather than the pulse width is important [66].

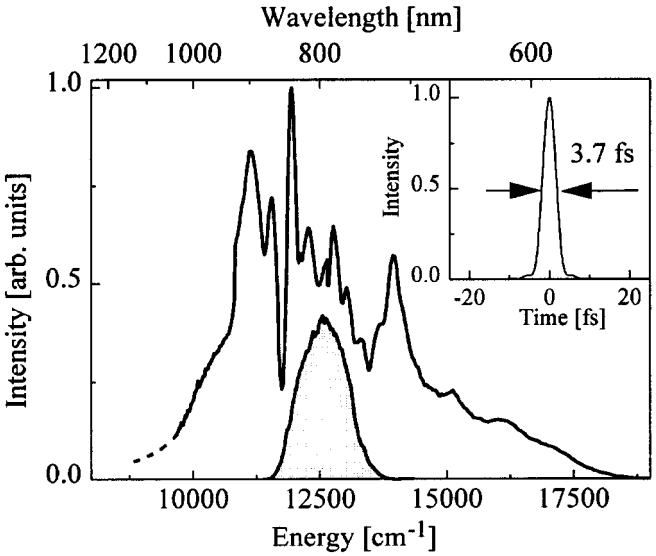

Fig. 2. Fiber-output (*solid line*) and cavity-dumped laser (*filled contour*) spectra. The inset shows the pulse obtained by Fourier transforming the fiber output spectrum, constant spectral phase assumed

2 Measurement of spectral phase

Pulse compression is used for the removal of spectral phase distortions accumulated by self-phase-modulation and propagation through dispersive media. Precise knowledge of the phase characteristics of a chirped pulse is therefore vitally important to the design of an appropriate pulse compressor. In order to fully characterize a pulse one needs to know its spectrum $I(\omega)$ and spectral phase $\varphi(\omega)$ or its time-dependent intensity $I(t)$ and temporal phase $\varphi(t)$. The temporal and spectral descriptions are complementary and follow from each other by Fourier transformation. Since no detector is fast enough to resolve the temporal shape of a pulse on a fs time scale, indirect methods have to be used to resolve the temporal shape of a fs pulse.

In recent years a number of techniques of indirect phase and pulse-shape retrieval have been proposed [67–78]. For instance, in various implementations of frequency-resolved optical gating (FROG, see for example [71–73]) a spectrally dispersed signal of autocorrelation-type is recorded. When a well-known phase-retrieval algorithm is used to analyse FROG traces, $I(t)$ and $\varphi(t)$ can be recovered.

Another approach to phase retrieval is spectrally-resolved up-conversion [25, 68–70, 75, 76, 78]. In this method, the analysed pulse (further called the probe pulse) is mixed with a well-characterized reference pulse in a nonlinear crystal. The resulting signal at the sum frequency is dispersed through a monochromator and can be expressed as

$$S(\Omega,\tau) \propto R(\Omega)\Omega^2 \left| \int_{-\infty}^{\infty} E_\mathrm{r}(\omega) E_\mathrm{p}(\Omega-\omega) \mathrm{e}^{\mathrm{i}\omega\tau} \frac{\mathrm{e}^{\mathrm{i}\Delta k(\Omega,\omega)L}-1}{\Delta k(\Omega,\omega)L}\,\mathrm{d}\omega \right|^2 , \quad (1)$$

where $R(\Omega)$ stands for the spectral sensitivity of the detector, $E_\mathrm{r}(\omega) = A_\mathrm{r}(\omega)\exp[\mathrm{i}\varphi_\mathrm{r}(\omega)]$ and $E_\mathrm{p}(\omega) = A_\mathrm{p}(\omega)\exp[\mathrm{i}\varphi_\mathrm{p}(\omega)]$ are the (complex) amplitudes of the reference and probe pulses, respectively, τ is a delay between them, and L is the

interaction length. The phase mismatch for type 1 (oo→e) interaction [79] is given as

$$\Delta k(\Omega,\omega) = k_{\mathrm{o}}(\Omega-\omega) + k_{\mathrm{o}}(\Omega) - k_{\mathrm{e}}(\Omega)\,, \tag{2}$$

with k denoting the wavevectors for ordinary (o) or extraordinary (e) waves. As in FROG, the cross-correlation signal $S(\Omega, t)$ contains explicit information about the complex electric field of the probe pulse, provided that the reference pulse has been fully characterized.

A valuable asset of the spectrally-resolved up-conversion technique is that in some special cases a time-consuming algorithm of phase retrieval can be replaced by a straightforward analysis. For instance, if the spectrum of the reference pulse is sufficiently narrow and its spectral phase is constant, (1) simplifies significantly and becomes

$$S(\Omega,\tau) \propto R(\Omega)\Omega^2 \operatorname{sinc}^2\left[\frac{[k_{\mathrm{o}}(\Omega-\omega_{\mathrm{r}}) + k_{\mathrm{o}}(\omega_{\mathrm{r}}) - k_{\mathrm{e}}(\Omega)]L}{2}\right] A_{\mathrm{p}}^2(\Omega-\omega_{\mathrm{r}}) A_{\mathrm{r}}^2\left(\tau - \frac{\mathrm{d}\varphi_{\mathrm{p}}(\Omega)}{\mathrm{d}\omega}\right)\,, \tag{3}$$

where $A_{\mathrm{r}}(t)$ stands for the temporal amplitude of the reference pulse. Note that the magnitude of the measured signal is proportional to Ω^2 [80]. This often-omitted factor gains importance with increased spectral bandwidth of the probe pulse.

Equation (3) shows that if the delay τ is scanned for a given setting of a monochromator Ω, the maximum of the up-converted signal directly reflects the group delay of the probe field [75]:

$$\tau_{\mathrm{p}}(\Omega = \omega_{\mathrm{p}} + \omega_{\mathrm{r}}) = \frac{\mathrm{d}\varphi_{\mathrm{p}}(\omega_{\mathrm{p}})}{\mathrm{d}\omega}\,. \tag{4}$$

Another important trait of spectrally-resolved up-conversion is that no factor limiting the acceptance bandwidth, such as phase-matching or the spectral response of a detector, influences the position of the maxima. These factors affect only the signal intensity. Furthermore, the phase-matching conditions are also relaxed for spectrally-resolved up-conversion compared to second-harmonic FROG, because the necessary acceptance bandwidth of the crystal is smaller by a factor of approximately two.

The spectral phase of the chirped white light is readily obtained from $\tau_{\mathrm{p}}(\Omega)$ by integration of (4):

$$\varphi_{\mathrm{p}}(\omega) = \int \tau_{\mathrm{p}}(\omega)\,\mathrm{d}\omega \tag{5}$$

The aforementioned technique is valid for reference pulses whose spectral bandwidths are appreciably narrower than those of the probe pulse. However, if a spectrally infinitely narrow pulse is chosen, the duration of the up-converted signal becomes infinitely long, limiting the time resolution. In the other extreme limit, when an infinitely short reference pulse is used, the up-converted signal is detected with an infinitely broad spectrum, limiting the resolution in the frequency domain. Therefore, there is an optimal reference-pulse duration that yields a compromise between temporal and spectral resolution.

In our experiment we cross-correlated the chirped white-light pulse with a laser pulse from the output coupler (shown as a solid arrow through the OC in Fig. 1) in a 100-μm-thick BBO crystal. The importance of having an independent reference beam at 82 MHz from the laser now becomes evident. This pulse has a suitable duration and spectral width for the reference pulse in the cross-correlation experiment. In order to have this pulse chirp-free, it was passed through a 4-prism compressor. The interferometric autocorrelation of this pulse was found to be in excellent agreement with the one calculated from the pulse spectrum by assuming a constant spectral phase.

To measure the group delay across the continuum, the up-converted signal was scanned as a function of the time delay between the white light and reference pulse at different wavelengths selected by a monochromator. The lay-out of this experiment is shown in the inset to Fig. 3. The spectral resolution of the monochromator was ~ 1 nm. The limited

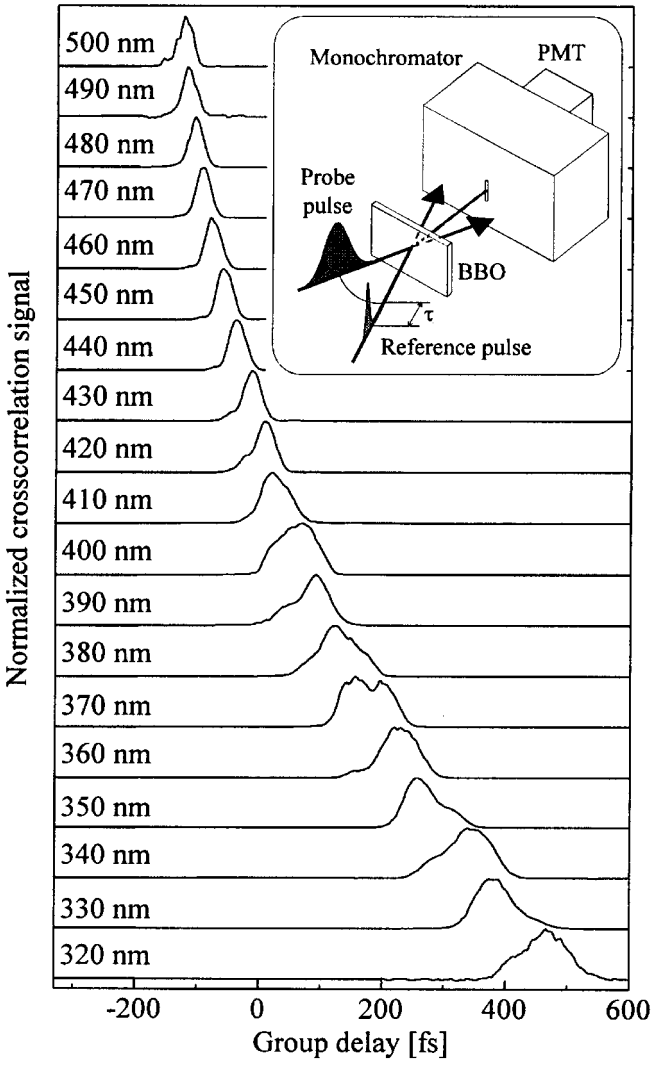

Fig. 3. Normalized probe-reference correlation signals at different wavelengths. The monochromator settings are indicated on the left of each trace. The schematic of the cross-correlation experiment is shown in the inset. Probe pulse stands for the white-light continuum, the reference pulse at 82-MHz repetition rate is derived directly from the Ti:sapphire laser. PMT photomultiplier tube

phase-matching bandwidth of the crystal meant that small angular tuning was necessary to obtain reliable measurements of the infrared and the visible components of the white-light spectrum. Typical normalized up-converted profiles at different settings of the monochromator are depicted in Fig. 3. The corresponding frequencies of the white light can be obtained when the central wavelength of the reference pulse (800 nm) is known. The duration of the up-converted signals increases toward the blue-shifted wing of the continuum. This is explained by a faster change in the spectral phase of the probe pulse within the spectral width of the reference pulse, compared to the relatively slowly changing phase in the infrared region, where material dispersion is considerably lower. The modulation appearing in some profiles is due to intensity variations in the spectrum around the central frequency of the continuum (Fig. 2). The up-converted signals cover the fundamental wavelengths of the white-light from 0.55 to 1.2 μm. Note that the bandwidth of the white-light that can be up-converted stretches much further into the infrared region than can be reliably measured (Fig. 2) by using a silicon photodiode array. This means that the real bandwidth of the white-light continuum and the shortest achievable pulse duration (Fig. 2, inset) are most probably underestimated.

To obtain the group delay across the white-light spectrum, weighted averages of the time-dependent up-converted traces were found. There are two reasons why this approach is superior to the evaluation of $\tau(\omega)$ from the peak positions as given by (4). First, the actual peak positions might be additionally shifted because of the unevenly distributed spectral intensity in the probe pulse. Second, by calculating weighed averages one uses the information from all experimental points and not only from the maxima [69, 70, 78]. The group delay of the white-light continuum is shown in Fig. 4 as solid points. The solid line represents a low-order polynomial fit used in calculations of the pulse compressor. The estimated group delay dispersion is $\sim 380\ \mathrm{fs}^2$ at the wavelength of 600 nm and decreases to $\sim 220\ \mathrm{fs}^2$ at 1 μm. We will return to the discussion of the apparent nonlinearity in the group delay in Sect. 4.

In closing this section we note that the measurements described in it were repeated several times with slightly different fiber lengths. The results were found to be identical – within experimental uncertainty – to those presented in Figs. 3 and 4, which indicates a remarkable long-term stability of the spectral phase.

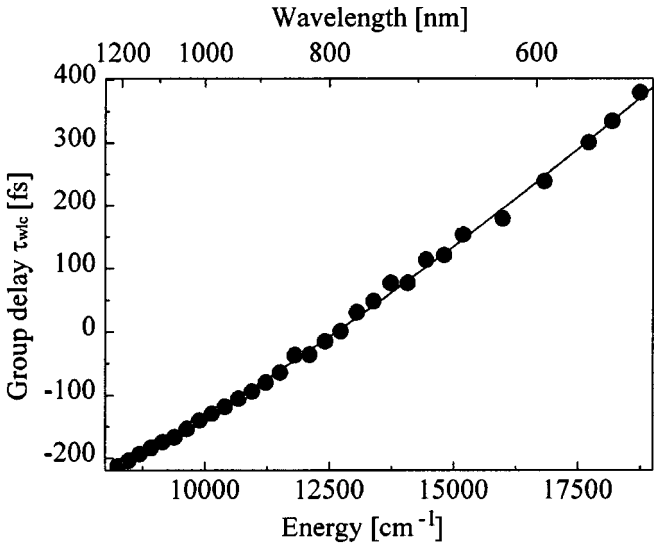

Fig. 4. Group delay of the white-light continuum retrieved from the probe-reference cross-correlations. Solid circles denote the first momenta of the up-converted temporal profiles and the solid line is a polynomial fit to the experimental points

3 Temporal analysis of the white light

To verify the group delay measurements, we studied the properties of the white-light continuum in the time domain. The temporal profile of the pulse and its instantaneous frequency, obtained by Fourier transformation of the electro-magnetic field, taking into account the spectral phase calculated according to (5), is shown in Fig. 5. The electromagnetic field is derived from the spectrum of the continuum (Fig. 2). Negative times represent the leading and positive times the trailing edge of the pulse. Note that the direction of time is unambiguous because no time-reversal symmetry is present in a cross-correlation experiment. Since the red-shifted components of the spectrum are concentrated in the leading edge of the pulse and the blue-shifted ones are trailing behind, we observe the usual chirp characteristics for pulse propagation in the normal dispersion regime. The asymmetry of the pulse and its spectrum will be addressed in more detail in the following section.

To probe the temporal shape of the pulse, the continuum is mixed with the reference pulse in a 15-μm-thick BBO crystal and the up-converted signal is detected by using a photomultiplier tube (PMT) [17, 81, 82]. The measured signal is displayed in Fig. 6 (open circles). In comparing this experimental pulse shape with the calculated one, several factors should be taken in consideration. First, the finite duration of the reference pulse needs to be taken into account. Second, the spectral response of the detector and the relevant phase-match conditions must be regarded. The up-converted signal

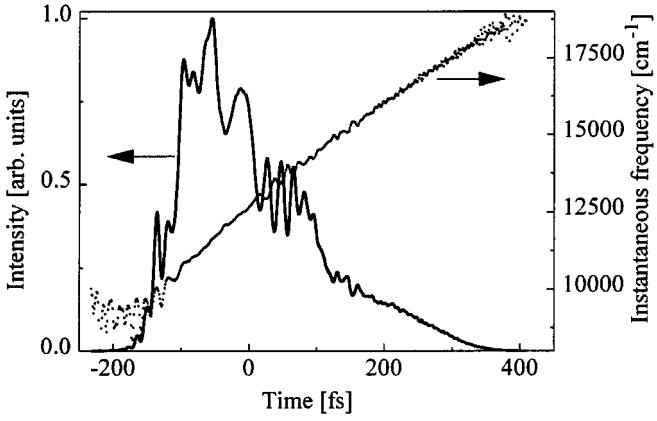

Fig. 5. Calculated temporal intensity (*solid line*) and chirp (*dotted line*) of the white-light continuum

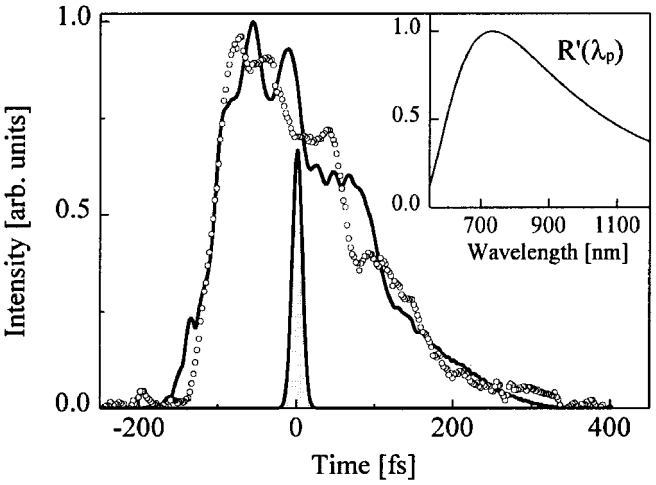

Fig. 6. Comparison of the experimental (*open circles*) and computed (*solid line*) cross-correlation between the white-light continuum and the reference pulse (*filled contour*). The solid curve was obtained by numerical correlation of the reference pulse with the white-light pulse and corrected for the spectral sensitivity $R'(\lambda_p)$. The overall spectral response of the detector and up-conversion efficiency of a 15-μm BBO crystal is displayed in the inset

can be calculated by integration of (3) over frequency:

$$S_{CC}(\tau) = \int_{-\infty}^{\infty} S(\Omega, \tau)\, d\Omega\,. \tag{6}$$

Taking into consideration the fact that the probe pulse is spectrally narrower than the white-light continuum, we may assume that each given instant corresponds to a single instantaneous frequency. In this approximation, (6) and (3) yield

$$S_{CC}(\tau) \propto R'\left(\omega_p(\tau)\right) \int_{-\infty}^{\infty} \left|E_p(t)\right|^2 \left|E_r(t-\tau)\right|^2 dt\,, \tag{7}$$

where $\omega_p(\tau)$ denotes the instantaneous frequency of the probe field as depicted by the dotted line in Fig. 5 and the overall spectral sensitivity is

$$R'\left(\omega_p(\tau)\right) = R\left(\omega_r + \omega_p(\tau)\right)\left[\omega_r + \omega_p(\tau)\right]^2 \operatorname{sinc}^2 \frac{\left[k_o\left(\omega_p(\tau)\right) + k_o(\omega_r) - k_e\left(\omega_r + \omega_p(\tau)\right)\right] L}{2}\,. \tag{8}$$

The correction term $R'(\omega_p)$, comprising a spectrally varying conversion efficiency, the phase-matching factor of the crystal, and the spectral response of the PMT, is depicted in the inset to Fig. 6. The main spectral distortions occur at the high-frequency part of the white-light continuum (i.e. in the trailing edge) where phase-mismatch in the non-linear crystal increases owing to the increased dispersion. The resulting temporal shape of the continuum calculated according to (7) is depicted in Fig. 6 as a solid line, and agrees reasonably well with the experimentally measured data, given all the assumptions made. This also indicates that the spectral phase was measured correctly. Comparison of the profiles of the chirped pulses in Figs. 5 and 6 shows also that a frequency-unresolved cross-correlation may deviate appreciably from the true pulse profile because of the spectral filtering effect.

4 Fiber output: experiment vs. numerical simulations

In a single-mode fiber, spectral broadening occurs because of the self-phase-modulation (SPM), whereas a combination of SPM and normal (or positive) group velocity delay (GVD) acts to smoothen the chirp [19]. The dynamic evolution of a pulse propagating in a single-mode fiber is described by the nonlinear Schrödinger equation (NSE) [83]. When only SPM and group delay dispersion are considered, the solution of the NSE yields a symmetric power spectrum, which corresponds to a symmetric rectangular-like pulse in the time domain and an almost linear chirp over most of the pulse duration [19]. It has been shown that linear frequency chirp, corresponding to a parabolic spectral phase, can be compensated by a quadratic compressor [19].

However, experiments [22] and numerical studies [84–88] have shown that higher-order dispersion and nonlinearities become increasingly important for propagation of femtosecond pulses, even for fibers shorter than 1 cm. In order to account for the intensity dependence of the group velocity, the conventional NSE should be extended to include a nonlinear correction term involving the time derivative of the pulse envelope, the so-called optical shock term [84]. This means that the part of the pulse that has the highest peak intensity, moves at a lower speed than the low-intensity wings. This effect, called self-steepening, causes pulse asymmetry and has been widely discussed in the literature (see, for example, Chap. 4 of [83] and the references therein). In the absence of mechanisms that stabilize this self-steepening process, it leads to an infinitely sharp pulse edge which creates an optical shock, similar to the development of an acoustic shock on the leading edge of a sound wave. Moreover, in this case the spectral phase of the pulse undergoes fast fluctuations which are difficult to compensate in a compressor.

Significant progress in numerical modelling of pulse propagation in fibers was made by taking into consideration *both* the optical shock term and higher-order dispersion [84–87]. It was shown that these two effects acting together suppress severe oscillations in the chirp. The predicted strongly asymmetric pulse shape and power spectrum agree reasonably well with the measured properties of our white-light pulse[2]. The nonlinearity of the chirp near the leading edge of the pulse fully agrees with our measurements. It is worth noticing that despite the fact that the spectrum is asymmetric, the bandwidth introduced by the higher-order terms can effectively be used to obtain pulses shorter than those from the purely SPM-broadened spectra [87].

5 Compressor design

A light pulse broadened by SPM action in a fiber and by propagation through bulk material can be compressed by passing it through a suitable optical element with anomalous (or negative) dispersion [89]. The group delay (or the spectral phase) is conventionally expanded into a Taylor series around

[2]The results of simulations most relevant to our experiments are presented in [86] in Fig. 2 (pulse shape and chirp) and Fig. 12 (pulse spectrum and spectrum phase)

a central frequency ω_0 [25]:

$$\tau(\omega) = \frac{\mathrm{d}\varphi(\omega_0)}{\mathrm{d}\omega} \cong \varphi''(\omega_0)(\omega-\omega_0) + \frac{1}{2}\varphi'''(\omega_0)(\omega-\omega_0)^2 + \frac{1}{6}\varphi''''(\omega_0)(\omega-\omega_0)^3 + \ldots , \quad (9)$$

where $\tau(\omega)$ is the group delay, $\varphi''(\omega_0)$ is the group delay dispersion (GDD), $\varphi'''(\omega_0)$ is the third-order dispersion (TOD), $\varphi''''(\omega_0)$ is the fourth-order dispersion (FOD), etc. Note that a constant (non-frequency-dependent) group delay has been disregarded in (9). This equation shows that in first order one should match the GDD of the compressor to the GDD of the pulse, in second order the TOD of the pulse and compressor should be matched, and so on.

The quest for optical pulse compression emerged soon after the invention of sub- nanosecond lasers. The first report on extracavity pulse compression concerned a mode-locked He-Ne laser [90]. Over the past three decades a number of compressors have been proposed and successfully implemented: resonant Gires–Tournois interferometers (GTIs) [91], resonant vapour delay lines [17], diffraction gratings [20, 92], and prism pairs [10, 23]. In particular, a combination of gratings and prisms [24, 25] was triumphantly used to achieve 6-fs pulses [25]. This compressor can compensate for both GDD and TOD over a very broad spectral range [93]. Recently, chirped mirrors [94] revolutionized the technology of ultrashort pulse generation.

Design of an appropriate high-throughput pulse compressor becomes increasingly difficult for larger bandwidth of the chirped pulse. In addition, the spectral region over which any of the aforementioned compressors provides adequate phase compensation narrows rapidly with increasing chirp rate. The requirements for compression of the white-light continuum arise from the fact that both GDD and TOD are positive, as is evident from Fig. 4. Therefore, one should aim for a compressor that exhibits both negative GDD and negative TOD. In our previous paper [50], we reported that the spectral range of the prism-grating compressor can be broadened by careful balancing the GDD against the FOD, such that nearly transform limited 5-fs pulses were obtained. This seems to represent the current limit of this technique for pulses chirped in a fused-silica fiber. Moreover, an oscillatory residual phase remained – as a trade-off between phase corrections of different orders – which led to sidelobes on the 5-fs pulse. Another inherent drawback of the grating-prism compressor is its low throughput, typically $\sim 25\%$ [50]. Note that the 200-nm bandwidth of recently designed high-efficient ($\sim 90\%$) gratings [95] is not sufficient for pulse compression down to 5-fs.

A major advance in pulse-compression technology was made by the introduction of a compressor based on chirped

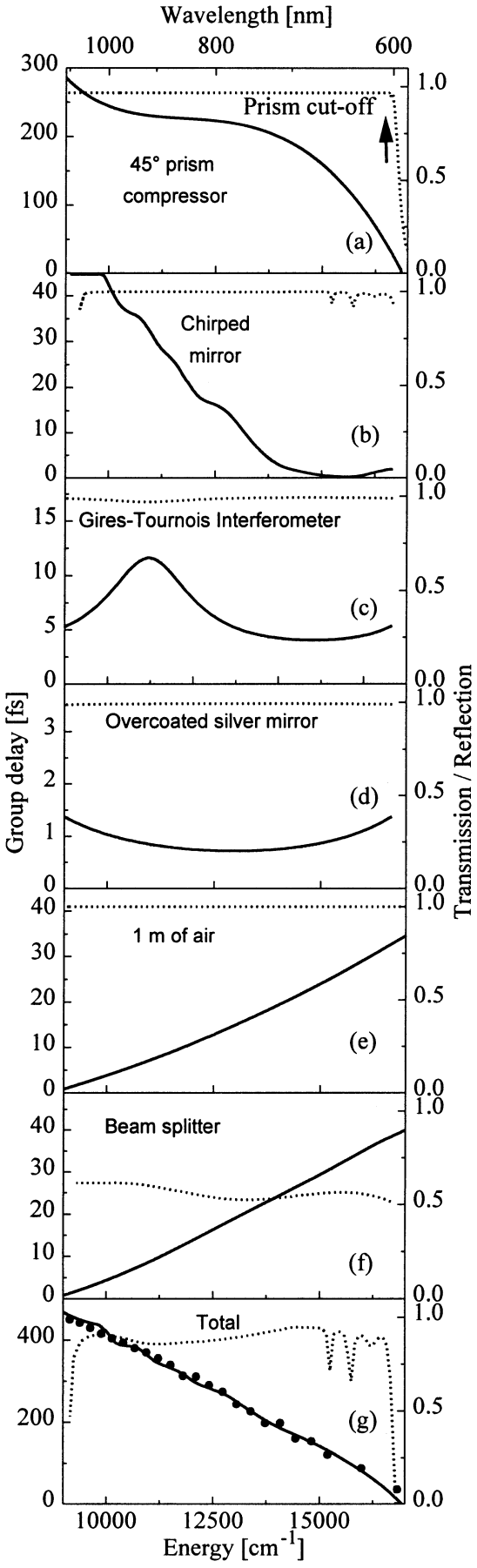

Fig. 7a–g. Overview of optical elements used in the compressor and autocorrelator: **a** 45° fused silica prism compressor, (**b**) chirped mirror, (**c**) Gires-Tournois interferometer, (**d**) overcoated silver mirrors, (**e**) 1 m of air, (**f**) beam splitter in the autocorrelator, and (**g**) total compressor. Group delays of various dispersive components are indicated by solid lines (left axis) and dotted lines show transmittance or reflectance (right axis). The compressor itself comprises three parts: a prism pair, chirped mirrors, and Gires-Tournois interferometers. Solid circles in (**g**) are the experimentally measured group delay depicted with the reversed sign and used as the desired group delay of the compressor. Reflection on the beam splitters is not taken into account in the overall throughput. The interprism pathlength in air is included in the prism compressor

mirrors and prisms [96]. In contrast to gratings, chirped mirrors can be made that have a large acceptance bandwidth and a very high reflectivity at the same time. With this prism–chirped-mirror compressor, pulses of 20-fs were amplified to the mJ level [97]; more recently a similar compressor was used to generate 5.5-fs, 6-nJ pulses at 1-MHz repetition rate [50] and sub-5-fs, 20-μJ pulses at a 1-kHz repetition rate [51].

To improve on our previous compression scheme [50], we designed a novel high-throughput compressor. To obtain the required negative GDD and FOD a fused-silica prism compressor was used (Fig. 7a), which, however, overcompensates the TOD when used alone. Recently it was shown that ultrabroadband chirped mirrors can be made that exhibit negative GDD and positive TOD (Fig. 7b), while having a reflectivity exceeding 99% over a bandwidth of 600–1100 nm [63, 98]. This means that a combination of chirped mirrors and a prism compressor provides flexible control over TOD across a large spectral range [63]. For higher-order phase corrections, broadband dielectric GTIs [99–101] have been shown to be suitable (Fig. 7c). GTIs counteract the FOD of the prism pair, which becomes significant above 900 nm. These ideas lead us to design a compressor that consists of a prism pair, ultra-broadband chirped mirrors, and dielectric GTIs.

We employed dispersive ray-tracing analysis [93, 102] to compute the group delay of the three-stage compressor. Use of (9) to calculate the spectral phase by a Taylor expansion becomes impractical since the compressor should span the region from 600 to 1100 nm. Wavelength-dependent refractive indices were calculated from dispersion equations and the corresponding refraction angles in the prism compressor were obtained by using Snell's law. Subsequently, the total accumulated phase of the prism compressor and bulk material was computed at each wavelength. By numerical differentiation of the phase, the group delay of the prism part of the compressor was obtained. This group delay was added to the group delay of the reflective optics to compute the overall group delay of the compressor. The resulting group delay τ_{COMPR} is then compared to the measured group delay of the white-light continuum τ_{WLC}, but taken with opposite sign. Subtracting the calculated group delay from the desired, we find the residual group delay

$$\tau_{\mathrm{RES}}(\omega) = \tau_{\mathrm{COMPR}}(\omega) - \tau_{\mathrm{WLC}}(\omega) \,, \tag{10}$$

which we integrate to obtain the residual spectral phase $\varphi_{\mathrm{res}}(\omega)$. To further characterize the compressor performance, the input white-light spectrum (Fig. 2) modified by the compressor throughput (Fig. 7, dotted curves) is calculated. With the residual phase taken into account, the temporal shape and phase of the compressed pulse is then computed via a Fourier transformation.

An overview of all optical elements used in the compressor and autocorrelator is presented in Fig. 7. The previously employed [50] unprotected gold-coated mirrors with 90% peak reflectivity and rapidly growing absorption below 600 nm, were substituted by low-dispersion and higher-reflectivity overcoated silver mirrors (Fig. 8d). The dispersion due to propagation in air [103] was also found to play an essential role for 5-fs pulses (Fig. 7e).

The compressor performance is optimized by varying the number of reflections on the dispersive mirrors, by changing the interprism spacing, and by varying the prism apex angles. Optimal performance is judged by looking for the shortest pulse through second harmonic generation in the autocorrelator. Hence, the pathlength in air from the compressor output, the 0.5-mm-thick beam splitter at 45° incidence (Fig. 7f), and reflections from the autocorrelator mirrors should be included in the calculations as well. Pulse broadening due to dispersion inside the autocorrelator nonlinear crystal was not considered because of its negligible effect. Reflectivity curves (Fig. 7, dotted lines) and group delays (Fig. 7, solid lines) of the chirped mirrors, GTIs, the overcoated silver mirrors, and beam splitters were provided by the manufacturer (R&D Lezer-Optika, Hungary).

The angle of incidence onto the fused-silica [104] prism, being a sensitive parameter, was chosen to correspond to the angle of least deviation for the sake of experimental convenience. Simulations show that apex angles smaller than 45° are impractical because they call for unreasonably large interprism separation. Moreover, with increased prism separation the positive dispersion of air (Fig. 7e) between the prisms becomes more important so that the whole compressor would need to be put in a vacuum. Note that the amount of the TOD could also be reduced by employing doubled-prism pairs, as has been demonstrated previously [51, 58].

Optimal compression (Fig. 7g) was obtained for five reflections from the chirped mirrors, two reflections from the GTI mirrors, and a 45° prism compressor with the following settings: ~ 5.2 mm of prism material for the 800-nm-wavelength ray and ~ 115 cm distance between apices. The root-mean-square error of the residual group delay amounts to ~ 1.5 fs. The blue wavelength cut-off of the prism compressor coincides with the abrupt reflectivity drop of the chirped mirrors, thus no additional loss of the spectral content originates from the prism part of the compressor. The compressor throughput is fairly flat between 600 and 1100 nm and amounts to $\sim 75\%$, mainly due to eight reflections from the non-Brewster-angle prisms. When a low-dispersive antireflection coating is deposited on the surfaces of the prisms, the total compressor throughput should reach $\sim 90\%$.

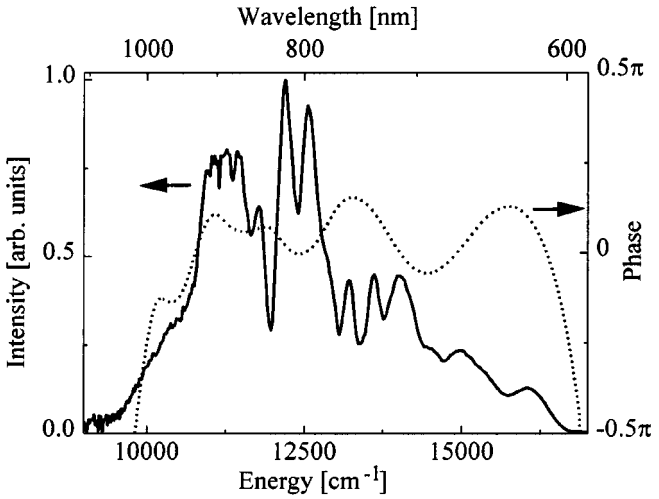

Fig. 8. Measured white-light continuum spectrum exiting the compressor (*solid line*) and calculated residual spectral phase of the compressed pulse (*dotted line*)

The measured spectrum and calculated residual phase of the white-light continuum passed through the compressor are presented in Fig. 8. The Fourier transform of this spectrum with constant phase assumed yields a pulse of ~ 4.5 fs in duration, i.e. somewhat longer than the Fourier transform of the input spectrum (Fig. 2, inset). This lengthening of the pulse occurs due to the loss of spectral components in the near infrared and visible part of the continuum. The residual phase falls within $\pm\pi/4$ limits for most of the spectral region. The oscillations of the phase around 700 nm are connected to the trade-off between higher-order dispersions of the chirped mirrors and prism pair. Residual phase correction should be feasible by installation of a programmable phase mask [105] into the pulse compressor. The applicability of this technique has recently been demonstrated for pulses as short as 10 fs [106]. Spectral shaping would also allow manipulating of the spectrum leading to cleaner optical pulses [107].

With the compressor being set up near the cavity-dumped laser and white-light generator (Fig. 1) the overall size of the system is 1 m $\times$ 1.5 m. This compactness makes our sub-5-fs laser system extremely robust and ensures cavity alignment for a long time. At laser startup the only thing needed is correction for the sub-micron drift of the fiber tip. The short warming-up time of the diode-pumped "Millennia" means that the stable regime of sub-5-fs operation is achieved within minutes. The compactness of the laser source presents a distinct advantage in experiments because it allows the experimental set-up to be close to the laser and thereby limits the amount of pulse propagation through air.

6 Pulse-duration measurement

Accurate pulse-width measurement of pulses containing only a few oscillations is quite a challenge. An easy and informative method used to judge the compression quality is the second-order interferometric autocorrelation (IAC) [89, 108]. An additional benefit from this technique is that it can be used as an on-line tool. Of course, the technical demands made on a 5-fs autocorrelator are substantial. In our experiments we employ a Mach–Zehnder interferometer [50, 109–111], which has the advantage of being fully symmetric with respect to both arms. Note that the "magic" 0 : 1 : 8 ratio between the minimum, asymptotic level, and maximum of the IAC trace [108] is obtained only if the intensities of the two interfering beams are strictly equal. If one intensity exceeds the other one by a factor of β, the renormalised ratio becomes $0 : [4 - 3\sqrt{\beta}/(1+\beta)] : 8$ with the asymptotic level being between 1 and 4. Imperfections in alignment of the interferometer lead to the same result.

The input beam is split and recombined in such a way that each of the beams travels once through an identical beam splitter and both reflections occur on the same coating–air interfaces (Fig. 9). To match the beam splitters [112], the initial horizontal polarization of the compressed pulse is rotated by a periscope. A 15-μm BBO crystal is used for second-harmonic generation. Such a thin crystal is required to avoid dispersion-induced pulse broadening and to ensure a sufficiently broad phase-matching bandwidth.

The moving arm of the interferometer is driven by a piezo transducer (PZT) controlled by a computer via a digital–analog convertor (DAC) and a high-voltage amplifier (HVA).

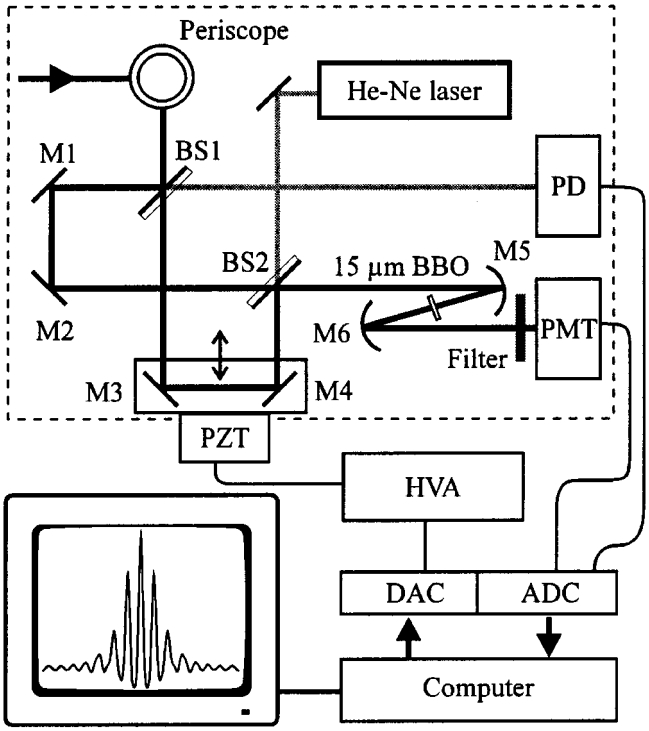

Fig. 9. Schematic of Mach–Zehnder interferometer for measurements of interferometric autocorrelation. BS1, BS2 50% ultra-broadband beam splitters centred at 800 nm; M1–M4 low-dispersion overcoated silver mirrors; M5 $r = -10$-cm, unprotected gold coated mirror; BBO 15-μm-thick BBO crystal; M6 $r = -10$-cm protected aluminium-coated mirror; PD photodiode; PMT photo multiplier tube; PZT piezo-electric transducer; HVA high-voltage amplifier; DAC digital–analog converter; ADC analog–digital converter. All optics were obtained from R&D Lezer Optika, Budapest

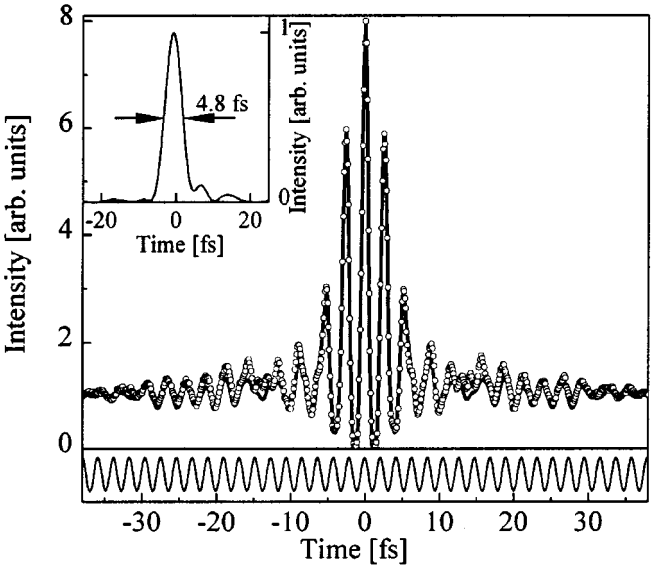

Fig. 10. Interferometric autocorrelation (IAC) of the compressed pulse. *Open circles* experimental points; *solid line* IAC calculated by Fourier transformation from the spectrum and predicted residual spectral phase. The corresponding pulse-intensity profile is shown in the inset. Bottom panel depicts He-Ne laser interference fringes used for on-line time calibration

After the M3–M4 arm is moved to a new position, the second-harmonic intensity is measurd by sampling and digitalizing the photomultiplier (PMT) signal. The experimental points obtained in this way are depicted in Fig. 10 by open circles. To introduce an on-line calibration of the time axis, a He-Ne laser beam is aligned in a direction opposite to the white light. The signal of the photodiode (PD) monitoring the interference fringes at the wavelength of the He-Ne laser [113] is used for precise time calibration (Fig. 10, lower panel).This allows autocorrelation measurements to be performed with ~ 0.2-fs accuracy throughout the whole scanning region of ~ 100-fs. A typical time step is ~ 0.1 fs, or 23 points per oscillation period at an 800-nm wavelength at the rate of ~ 60 ms for a 100-fs scan.

The typical IAC shown in Fig. 10 was obtained by setting the compressor according to the calculated optimal settings, after which the amount of prism material was balanced so as to get the shortest autocorrelation. Compared to our previous result [50], the wing structure of the IAC is substantially reduced, which demonstrates the superior characteristics of this compressor. We verified the importance of the GTIs for high-order dispersion correction by changing the angle of incidence from the design angle of 45° to $\sim 15°$. In this case the group-delay curve shifts towards shorter wavelengths (Fig. 7c), resulting in broadening of the central part of the IAC function and an appreciable increase in the amplitude of its wings.

When fitting the IAC to a hyperbolic secant envelope, we get a pulse of ~ 3.8 fs, whereas for a Gaussian a pulse of ~ 4.5 fs is obtained. The former value violates the spectrum-limited pulse duration of ~ 4.5 fs derived earlier (Sect. 5). Furthermore, neither of these pulse shapes reproduces the wing structure on the experimental IAC. This clearly indicates that one should be extremely cautious fitting the IAC of a short pulse to an a priori assumed pulse profile, especially when the pulse spectrum is not smooth. It should also be noted that the standard deviation, conventionally used in fitting routines to judge the fit quality [114], can hardly serve as a criterion in favour of any particular pulse shape. Most of the experimental points in the IAC are located at the slopes of the fringes where the gradient is too high for any anomaly to be recognized. As a matter of fact, only 8–10 points at the extrema of the IAC are meaningful, which is clearly not sufficient to discriminate between the different pulse profiles. We will return to the problem of retrieving the pulse shape from the IAC in the next section.

A good criterion for judging the accuracy of calculations of the phase of the compressor is to simulate the IAC by Fourier transforming the spectrum, taking into account the calculated residual phase (Fig. 8). The resulting trace, given as a solid line in Fig. 10, reproduces the experimental data remarkably well. The excellent agreement obtained validates our analysis of the phase characteristics of the compressor and underlines the correctness of the developed numerical routines. The corresponding temporal profile of the compressed pulse is presented in the inset to Fig. 10. The pulse duration amounts to ~ 4.8 fs FWHM, which corresponds to ~ 2.7 optical oscillations of the electric field at 780 nm wavelength. The oscillatory structure on the trailing edge of the pulse originates from the imperfection in the phase compensation around 700 nm (Fig. 8).

7 5-fs pulse reconstruction from the IAC and spectrum

In the previous section we showed that a fit of the interferometric autocorrelation (IAC) to an a priori analytical pulse-intensity profile is not warranted. Obviously, it would be a major step forward if the pulse shape could be retrieved from the IAC without us having to rely on any assumption concerning the temporal profile of the electric field. It was pointed out by Naganuma et al. [67] that information on the phase and amplitude of the pulse is, in principle, contained in the IAC and pulse spectrum. Recently, a robust algorithm that recovers this information from the autocorrelation was reported [115, 116]. In this section we apply this algorithm to the retrieval of the phase and pulse shape of the compressed pulse from the IAC.

The normalized interferometric autocorrelation signal can be expressed as [67]

$$\begin{aligned}\mathrm{IAC}(\tau) =& 1 + 2G(\tau) + 4\mathrm{Re}\left[F_1(\tau)\exp(\mathrm{i}\omega_0\tau)\right] \\ &+ \mathrm{Re}\left[F_2(\tau)\exp(-2\mathrm{i}\omega_0\tau)\right] ,\end{aligned} \tag{11}$$

where

$$G(\tau) = \int_{-\infty}^{\infty} I(t)I(t-\tau)\,\mathrm{d}t , \tag{12}$$

$$F_1(\tau) = \int_{-\infty}^{\infty} \frac{I(t)+I(t-\tau)}{2} E(t)E^*(t-\tau)\,\mathrm{d}t , \tag{13}$$

$$F_2(\tau) = \int_{-\infty}^{\infty} E^2(t)E^{*^2}(t-\tau)\,\mathrm{d}t . \tag{14}$$

Here $G(t)$ stands for the (background-free) intensity autocorrelation, and $F_2(t)$ represents the second-harmonic field

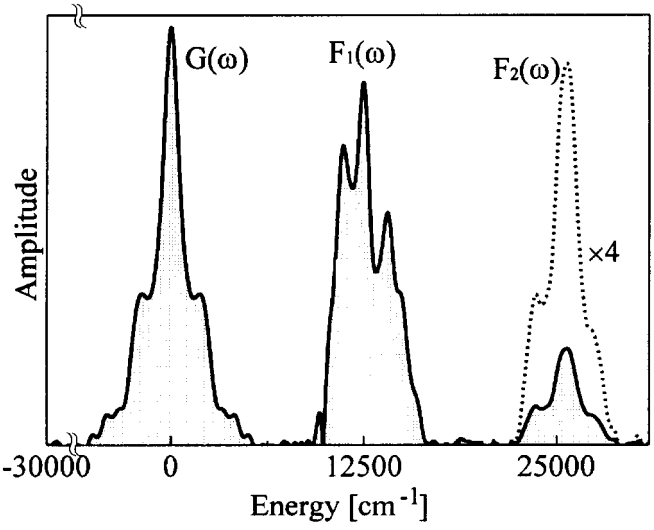

Fig. 11. Fourier transform of the experimental interferometric autocorrelation function. The mirror image of the spectrum at the negative frequencies is not shown. The close similarity between the zero and double-frequency peaks indicates that the compressed pulse is almost chirp-free

autocorrelation. Note that when the temporal phase is a constant the functions $G(t)$ and $F_2(t)$ become identical [67]. This property can be exploited to determine whether the compressed pulse carries any residual chirp. Since the carrier frequencies of $G(\tau)$ and $F_2(\tau)$ are different, the simplest way to extract this information from the IAC (Fig. 10) is to Fourier transform the IAC, with the constant background [1 in (11)] subtracted. One then obtains a spectrum composed of $G(\omega)$ at zero frequency, $F_1(\omega)$ at the fundamental frequency ω_0, and $F_2(\omega)$ at the second-harmonic frequency $2\omega_0$ (Fig. 11). Note that since the last two components are projected at both positive and negative frequencies, their magnitudes are reduced by a factor of 2 compared to the ratios given by (11). As can be seen from Fig. 11, the functions $G(\omega)$ and $F_2(\omega)$ are quite similar, which confirms our earlier conclusion that the compressor has removed most of the chirp in the white-light continuum. Nonetheless, the small asymmetry of $F_2(\omega)$ indicates that there is some residual chirp in the compressed pulse.[3]

Peatross et al. recently demonstrated temporal decorrelation of the intensity autocorrelation function [115]. Their idea based on the application of the Wiener–Khinchin theorem to $G(\tau)$ [117]:

$$G(\omega) = |I(\omega)|^2 , \tag{15}$$

where $I(\omega)$ and $G(\omega)$ are the Fourier-transforms of the pulse intensity $I(t)$ and the autocorrelation function, respectively:

$$I(\omega) = \frac{1}{\sqrt{2\pi}} \int_{-\infty}^{\infty} I(t) \mathrm{e}^{\mathrm{i}\omega t} \, \mathrm{d}t , \tag{16}$$

$$G(\omega) = \frac{1}{\sqrt{2\pi}} \int_{-\infty}^{\infty} G(\tau) \mathrm{e}^{\mathrm{i}\omega t} \, \mathrm{d}\tau . \tag{17}$$

It is evident from (15) that the function $G(\omega)$ contains no information on the phase $\Psi(\omega)$ of $I(\omega) = |I(\omega)| \exp[\mathrm{i}\Psi(\omega)]$.[4] However, since the pulse intensity $I(t)$ is *real, non-negative*, and *finite* in time, it can be shown [115, 116] that the intensity autocorrelation has a certain uniqueness. Information on the direction of time, which an autocorrelation lacks, could easily be obtained experimentally [72, 118, 119].

Figure 12 shows the computational scheme used to retrieve the shape and phase of the pulse. In the first loop, we use the algorithm proposed by Peatross et al. [115]. The input consists of the spectral intensity $I(\omega)$, calculated from the experimental autocorrelation according to (15) and an initial guess of the phase $\Psi(\omega)$. The Fourier transform into the time domain yields the temporal pulse intensity $I(t)$. Because $I(t)$ must be a non-negative function, all negative parts of $I(t)$ are set to zero. The resulting $I(t)$ is then Fourier transformed back into the frequency domain, yielding the next approximation to $\Psi(\omega)$. At this point, an iterative fitting procedure

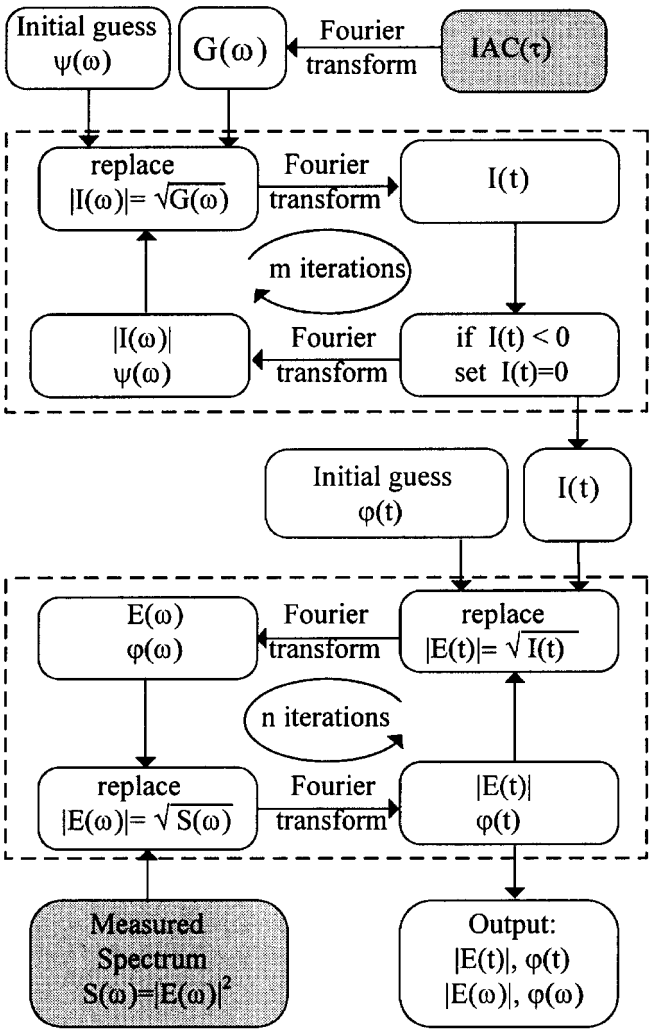

Fig. 12. Block diagram of the iterative algorithm for pulse shape and phase retrieval. Dashed rectangles represent two successive parts of the algorithm used to retrieve the pulse shape and the phase, respectively. The input of the algorithm is the zero-frequency spectrum of the interferometric autocorrelation $G(\omega)$ and the pulse spectrum $S(\omega)$ (*shaded boxes*)

starts, whereby in each consecutive round $|I(\omega)|$ is replaced by $[G(\omega)]^{1/2}$. Convergence is judged by comparison of the calculated and experimental autocorrelations or their Fourier transforms. In a number of simulations we found that the precision of the experimental data and sampling of time and frequency arrays used in the calculations are the major factors limiting the convergence of the algorithm. Note that no minimum phase assumption (as in [117]) has been made.

The pulse intensity $I(t)$ recovered in the first round is then injected into the second loop, which aims to recover the spectral and temporal phases of the pulse. The algorithm used here (Fig. 12, lower part) was developed by Gerchberg and Saxton [120]. It is based on the fact that the modulus of a complex field in the time domain, $|E(t) = [I(t)]^{1/2}|$ and a modulus of its Fourier transform $|E(\omega)| = [S(\omega)]^{1/2}$, where $S(\omega)$ denotes the power spectrum, uniquely define the full complex fields $E(t)$ and $E(\omega)$ in a majority of practical cases [121]. The algorithm employs a sequence of Fourier transformations with the spectral and temporal amplitudes being replaced by $[S(\omega)]^{1/2}$ and $[I(t)]^{1/2}$ on each consecutive run. The itera-

[3] Note that there is a distinct difference between transform-limited (or spectral-limited) and chirp-free pulses. For instance, in the case of an asymmetric spectrum, a transform-limited pulse does carry some chirp, even if its spectral phase is constant.

[4] The phase $\Psi(\omega)$ of the spectral intensity $I(\omega)$ should not be confused with the phase $\varphi(\omega)$ of the electrical field $E(\omega)$.

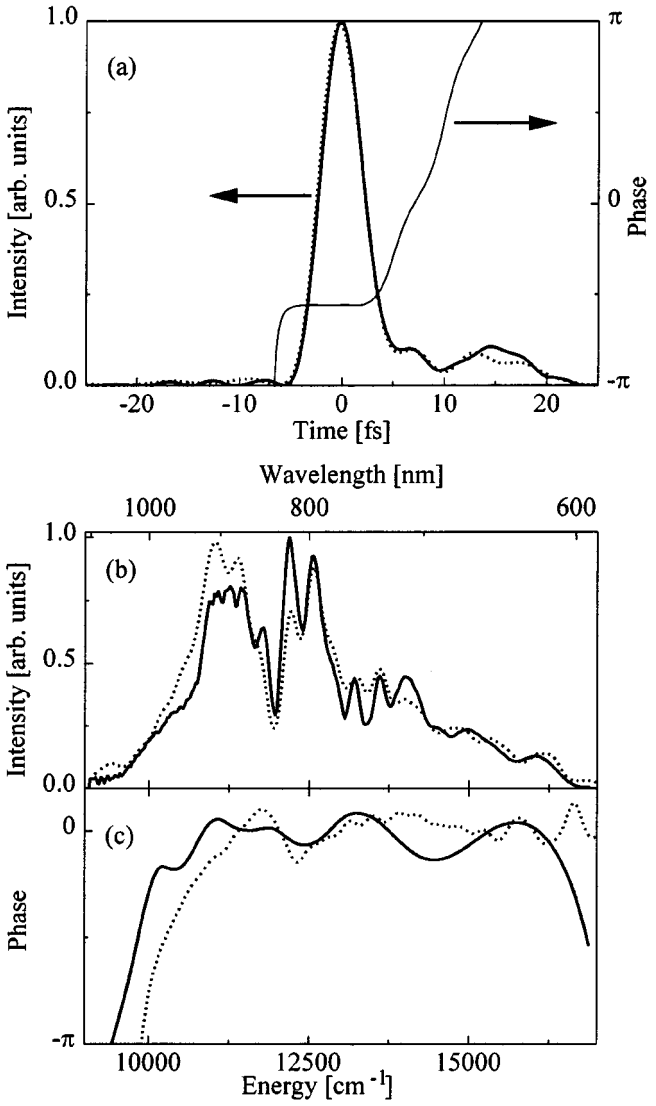

Fig. 13a–c. Output of the pulse-retrieval program. **a** - pulse intensity retrieved in the first loop (*solid line*) and recovered in the second loop (*dotted line*) of the iterative algorithm. Temporal phase (*thin line*) corresponds to the latter intensity curve. **b** - recovered spectrum (*dotted line*) and input spectrum (*solid line*). **c** - retrieved spectral phase (*dotted line*) and spectral phase resulting from compressor design (*solid line*)

tive procedure is halted when the difference between two subsequent iterations becomes negligibly small.

The solid line in Fig. 13a displays the pulse recovered from the IAC in Fig. 11. The pulse duration of 4.8 fs is identical to that obtained from phase calculations at the pulse compressor (Fig. 10, inset). Note that the wing structure on the trailing edge of the pulse is consistent with the predicted magnitude. The final results of the complete algorithm are presented in Fig. 13. The resulting temporal and spectral phases are depicted in Figs. 13a and 13c, respectively. In order to demonstrate the level of agreement between the input and output values of the algorithm, the temporal and spectral intensities (dotted lines in Figs. 13a and 13b), corresponding to the final iteration are plotted against the decorrelated pulse intensity and the spectral intensity (solid lines). The predicted residual phase of the compressor (solid line in Fig. 13c) agrees reasonably well with the phase rendered by the second loop of the algorithm. We obtain a pulse duration of ~ 4.8 fs for the decorrelated pulse in the first loop and ~ 4.9 fs for the output of the entire algorithm confirming the pulse duration and its shape derived in Sect. 6 (Fig. 10, inset).

8 Summary and future prospects

In this paper we have discussed a compact and robust light source that generates sub-5-fs, 2-MW pulses at variable repetition rates of up to 1 MHz, by using a novel three-stage compressor. The phase characteristics of the compressor have been analysed with dispersive ray-tracing and mapped onto the measured group delay of the continuum. The fidelity of this approach has been confirmed by the fact that the pulse shape derived from the optical spectrum and the calculated residual phase, fit the measured autocorrelation function very well. It has also been shown that the interferometric autocorrelation and optical spectrum of the compressed pulse comprised sufficient information to derive the temporal pulse intensity and its phase.

We foresee several applications of this ultrafast laser. First, it is an almost ideal tool for ultrafast spectroscopy, if not for the short pulse then for the white-light continuum that can be used as a probe for spectral events from the blue-green part of the spectrum to the near infrared region (500 nm to 1.3 μm). The large bandwidth of this laser may also be of use in optical coherence tomography measurements [66]. For the near future we aim for an all-chirped-mirror compressor, which would enable an even more compact design of this laser. With smaller diode-pumped light sources coming on the market there is every reason to believe that soon it will be possible to build a sub-5-fs cavity-dumped laser that fits onto a breadboard of only 1 m × 0.5 m. This may be an important asset for many applications.

We propose to use sub-5-fs pulses from this cavity-dumped laser in an ultrafast photon-echo study of the free electron in water. Pioneering optical studies started about ten years ago [122, 123] when optical pulses of about 100 fs became available in the wavelength region where the equilibrated aqueous electron absorbs (~ 800 nm). Following these experiments, several mixed quantum-classical molecular dynamical studies were performed on the electron-in-water system [124–126]. These investigations gave a clear picture of the energetics and dynamics of the aqueous electron, and provided a strong stimulus for new experiments. However, as the equilibration and solvation dynamics of the electron occur on a sub-100-fs time scale, a full characterization of the electron's dynamics has not been achieved yet [127].

The aqueous electron is one of the simplest physical systems to study, yet grasp of its dynamics at a fundamental level is extremely important. It is unique in the sense that it provides the opportunity to confront results of state-of-the-art nonlinear optical experiments with quantum molecular dynamics simulations. The wet electron is also relevant from a chemical point of view, as water is one of the most ubiquitous solvents in all of chemistry. Because water has a large dipole moment and exhibits strong hydrogen bonding, its dynamics is often strongly coupled to the reaction path, especially when a rearrangement of electronic charge takes place. Our laser system seems ideally suited, as the sub-5-fs

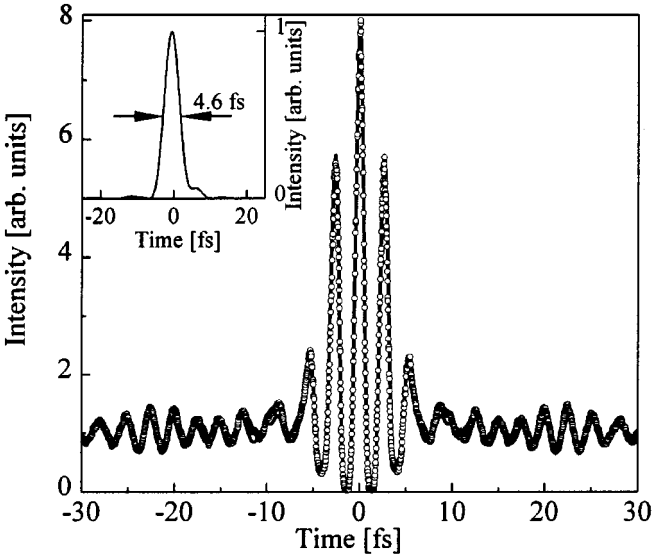

Fig. 14. Interferometric autocorrelation of a 4.6-fs pulse. *Open circles* experimental points, *solid line* calculated IAC of deduced pulse shape shown in the inset

pulse spectrum overlaps very nicely with that of the aqueous electron.

9 Note added

While this manuscript was under review, the pulse compressor was further improved by replacing the collimating lens by an off-axis parabolic mirror (Janos Technology). Because of reduced material dispersion the number of bounces on the chirped mirrors was also reduced and the interprism distance shortened. Furthermore, a different type of fiber (Newport F-SV) was found to generate an output mode of better quality. In addition, this fiber is much simpler to align since it does not require polarization matching. The resulting interferometric autocorrelation of the compressed pulses is displayed in Fig. 14. The derived pulse shape is depicted as inset in Fig. 14; the corresponding pulse width is deduced to be ~ 4.6 fs. Clearly, the wings of the pulse have been improved significantly, as is obvious from a comparison of Figs. 10 and 14. We have also shown that the interferometric autocorrelation of a sub-5-fs compressed pulse, similar to the one depicted in Fig. 14, can be obtained by measuring the two-photon-induced photocurrent [128, 129] in a GaP photodiode [130].

Acknowledgements. We acknowledge useful discussions with M. Joffre (ENSTA, Ecole Polytechnique) on spectral phase measurements using frequency-resolved up-conversion techniques. We are indebted to J. Peatross (Brigham Young University) for computational details on decorrelation and for permission to reproduce the algorithm schematic. We are also grateful to Andy Rundquist (University of Michigan, Ann Arbor) for drawing our attention to the Gerchberg–Saxton algorithm. A.B. and M.S.P. would like to thank R. Szipöcs and K. Ferencz (Research Institute for Solid State Physics, Budapest) for their hospitality during their visits to Budapest. We would also like to thank K. Ferencz for manufacturing the femtoseconds optics, I. Shumay (Universität Erlangen-Nürnberg, Erlangen) for recommending the "Millennia" as a pump laser for the cavity-dumped Ti:sapphire laser, and F. de Haan for development of the software for data collection and handling. The investigations were supported by the Netherlands Foundation for Physical Research (FOM) with financial aid from the Netherlands Organization for the Advancement of Science (NWO).

References

1. W. Kaiser (Ed.): *Ultrashort Light Pulses: Generation and Applications*, 2nd ed.(Springer, Berlin 1993)
2. A.H. Zewail: J. Phys. Chem. **100**, 12701 (1996) and references therein
3. N.W. Woodbury, M. Becker, D. Middendorf, W.W. Parson: Biochemistry **24**, 7516 (1985)
4. J.L. Martin, J. Breton, A.J. Hoff, A. Migus, A. Antonetti: Proc. Natl. Acad. Sci. USA **83**, 957 (1986)
5. G.R. Fleming: *Chemical Applications of Ultrafast Spectroscopy*, (Oxford University Press, New York 1986)
6. S. Mukamel: *Principles of Nonlinear Optical Spectroscopy*, (Oxford University Press, New York 1995)
7. R.L. Fork, B.J. Greene, C.V. Shank: Appl. Phys. Lett. **41**, 671 (1981)
8. J.P. Gordon, R.L. Fork: Opt. Lett. **9**, 153 (1984)
9. H. Avramopoulos, R.L. Fork: J. Opt. Soc. Am. B **8**, 117 (1991)
10. R.L. Fork, O.E. Martinez, J.P. Gordon: Opt. Lett. **9**, 150 (1984)
11. O.E. Martinez, R.L. Fork, J.P. Cordon: Opt. Lett. **9**, 156 (1984)
12. J.A. Valdmanis, R.L. Fork, J.P. Gordon: Opt. Lett. **10**, 131 (1985)
13. J.A. Valdmanis, R.L. Fork: IEEE J. Quantum Electron. **22**, 112 (1986)
14. A.H. Zewail: In *Femtosecond Reaction Dynamics* ed. by D.A. Wiersma (North-Holland, Amsterdam 1994), pp.1–28 and references therein
15. W.N. Knox, R.L. Fork, M.C. Downer, D.A.B. Miller, D.S. Chemla, C.V. Shank, A.C. Gossard, W. Wiegmann: Phys. Rev. Lett. **54**, 1306, (1985)
16. W.N. Knox, C. Hirlimann, D.A.B. Miller, J. Shah, D.S. Chemla, C.V. Shank: Phys. Rev. Lett. **56**, 1191 (1985)
17. H. Nakatsuka, D. Grischkowsky, A.C. Balant: Phys. Rev. Lett. **47**, 910 (1981)
18. R.R. Alfano, S.L. Shapiro: Phys. Rev. Lett. **24**, 592 (1970)
19. W.J. Tomlinson, R.H. Stolen, C.V. Shank: J. Opt. Soc. Am. B **1**, 139 (1984)
20. E. Treacy: IEEE J. Quantum Electron. **5**, 454 (1969)
21. J.-M. Halbout, D. Grischkowsky: Appl. Phys. Lett. **45**, 1281 (1984)
22. W.H. Knox, R.L. Fork, M.C. Downer, R.H. Stolen, C.V. Shank, J.A. Valdmanis: Appl. Phys. Lett. **46**, 1120 (1985)
23. Zs. Bor, B. Racz: Opt. Commun. **54**, 165 (1985)
24. J.D. Kafka, T. Baer: Opt. Lett. **12**, 401 (1987)
25. R.L. Fork, C.H. Brito Cruz, P.C. Becker, C.V. Shank: Opt. Lett. **12**, 483 (1987)
26. P.C. Becker, H.L. Fragnito, J.-Y. Bigot, C.H. Brito Cruz, R.L. Fork, C.V. Shank: Phys. Rev. Lett. **63**, 505 (1989)
27. J.-Y. Bigot, M.T. Portella, R.W. Schoenlein, C.J. Bardeen, A. Migus, C.V. Shank: Phys. Rev. Lett. **66**, 1138 (1991)
28. E.T.J. Nibbering, D.A. Wiersma, K. Duppen: Phys. Rev. Lett. **66**, 2464 (1991)
29. R.A. Mathies, C.H. Brito Cruz, W.T. Pollard, C.V. Shank: Science **240**, 777 (1988)
30. Q. Wang, R.W. Schoenlein, L.A. Peteanu, R.A. Mathies, C.V. Shank: Science **266**, 422 (1994)
31. D.E. Spence, P.N. Kean, W. Sibbett: Opt. Lett. **16**, 42 (1991)
32. Ch. Spielmann, P.F. Curley, T. Brabec, E. Wintner, F. Krausz: Electron. Lett. **28**, 1532 (1992)
33. C.-P. Huang, M.T. Asaki, S. Backus, M.M. Murnane, H.C. Kapteyn, H. Nathel: Opt. Lett. **17**, 1289 (1992)
34. B. Proctor, F. Wise: Appl. Phys. Lett. **62**, 470 (1993)
35. M.T. Asaki, C.-P. Huang, D. Garvey, J. Zhou, H.C. Kapteyn, M.M. Murnane: Opt. Lett. **18**, 977 (1993)
36. Ch. Spielmann, P.F. Curley, T. Brabec, F. Krausz: IEEE J. Quantum Electron. **30**, 1100 (1994)
37. A. Stingl, Ch. Spielmann, F. Krausz, R. Szipöcs: Opt. Lett. **19**, 204 (1994)
38. P. Moulton: J. Opt. Soc. Am. B **3**, 125 (1985)
39. J.P. Zhou, G. Taft, C.-P. Huang, M.M. Murnane, H.C. Kapteyn, I.P. Christov: Opt. Lett. **19**, 1149 (1994)
40. A. Stingl, M. Lenzner, Ch. Spielmann, F. Krausz, R.Szipöcs: Opt. Lett. **20**, 602 (1995)
41. A. Kasper, K.J. Witte: Opt. Lett. **21**, 1259 (1996)
42. L. Xu, Ch. Spielmann, F. Krausz, R. Szipöcs: Opt. Lett. **21**, 1259 (1996)

43. R. Fluck, I.D. Jung, G. Zhang, F.X. Kärtner, U. Keller: Opt. Lett. **21**, 743 (1996)
44. I.D. Jung, F.X. Kärtner, N. Matuschek, D.H. Sutter, F. Morier-Genoud, G. Hang, U. Keller, V. Scheuer, M. Tilsch, T. Schudi: Opt. Lett. submitted (1997)
45. I.P. Christov, M.M. Murnane, H.C. Kapteyn, J.P. Zhou, C.-P. Huang: Opt. Lett. **19**, 1465 (1994)
46. S.T. Cundiff, W.N. Knox, E.P. Ippen, H.A. Haus: Opt. Lett. **21**, 662 (1996)
47. M.S. Pshenichnikov, W.P. de Boej, D.A. Wiersma: Opt. Lett. **19**, 572 (1994)
48. M. Nisoli, S. De Silvestri, O. Svelto: Appl. Phys. Lett. **68**, 2793 (1996)
49. M.S. Pshenichnikov, A. Baltuška, Z. Wei, D.A. Wiersma: Proceedings of OSA Annual Meeting /ILS-XII (Rochester, October 20-24, 1996), postdeadline paper PD1
50. A. Baltuška, Z. Wei, M.S. Pshenichnikov, D.A. Wiersma: Opt. Lett. **22**, 102 (1997)
51. M. Nisoli, S. De Silvestri, O. Svelto, R. Szipöcs, K. Ferencz, S. Sartania, Ch. Spielmann, F. Krausz: Opt. Lett. **22**, 522 (1997)
52. M.S. Pshenichnikov, K. Duppen, D.A. Wiersma: Phys. Rev. Lett. **74**, 674 (1995)
53. W.P. de Boeij, M.S. Pshenichnikov, D.A. Wiersma: J. Phys. Chem. **100**, 11806 (1996)
54. C.J. Bardeen, Q. Wang, C.V. Shank: Phys. Rev. Lett. **75**, 3410 (1995)
55. W.S. Warren, H. Rabitz, M. Dahleh: Science **259**, 1581 (1993)
56. B. Kohler, V.V. Yakovlev, J. Che, J.L. Krause, M. Messina, K.R. Wilson, N. Schwentner, R.M. Whitnell, Y.J. Yan: Phys. Rev. Lett. **74**, 3360 (1995)
57. Y.R. Shen: *The Principles of Nonlinear Optics*, (Wiley, New York 1984)
58. B. Proctor, F. Wise: Opt. Lett. **17**, 1295 (1992)
59. M. Ramaswamy, M. Ulman, J. Paye, J.G. Fujimoto: Opt. Lett. **18**, 1823, (1993)
60. E.W. Castner Jr., J.J. Korpershoek, D.A. Wiersma: Opt. Commun. **78**, 90 (1990)
61. V. Magni, S. De Silvestri, A. Cyco-Aden: Opt. Commun. **82**, 137 (1991)
62. A. Cyco-Aden, M. Nisoli, V. Magni, S. De Silvestri, O. Svelto: Opt. Commun. **92**, 271 (1992)
63. E.J. Mayer, J. Möbius, A. Euteneuer, W.W. Ruhle, R. Szipöcs: Opt. Lett. **22**, 528 (1997)
64. M.S. Pshenichnikov, W.P. de Boeij, D.A. Wiersma, unpublished (1994)
65. G.N. Gibson, R. Klank, F. Gibson, B.E. Bouma: Opt. Lett. **21**, 1055 (1996)
66. D. Huang, E.A. Swanson, C.P. Lin, J.S. Schuman, W.G. Stinson, W. Chang, M.R. Hee, T. Flotte, K. Gregory, C.A. Puliafito, J.G. Fujimoto: Science **254**, 1178 (1991)
67. K. Naganuma, K. Mogi, H. Yamada: IEEE J. Quantum Electron. **25**, 1225 (1989)
68. J.L.A. Chilla, O.E. Martinez: IEEE J. Quantum Electron. **27**, 1228 (1991)
69. J. Paye: IEEE J. Quantum Electron. **28**, 2262 (1992)
70. J.-P. Foing, J.-P. Likforman, M. Joffre, A. Migus: IEEE J. Quantum Electron. **28**, 2285 (1992)
71. D.J. Kane, R. Trebino: Opt. Lett. **18**, 823 (1993)
72. J. Paye, M. Ramaswamy, J.G. Fujimoto, E.P. Ippen: Opt. Lett. **18**, 1947 (1993)
73. K.W. DeLong, R. Trebino, D.J. Kane: J. Opt. Soc. Am. B **11**, 1595 (1994)
74. B.S. Prade, J.M. Schins, E.T.J. Nibbering, M.A. Franco, A. Mysyrowicz: Opt. Commun. **113**, 79 (1994)
75. J.-K. Rhee, T.S. Sosnowski, T.B. Norris: Opt. Lett. **19**, 1550 (1994)
76. J.-K. Rhee, T.S. Sosnowski, A.-C. Tien, T.B. Norris: J. Opt. Soc. Am. B **13**, 1780 (1996)
77. E.T.J. Nibbering, M.A. Franco, B.S. Prade, G. Grillon, J.-P. Chambaret, A. Mysyrowicz: J. Opt. Soc. Am. B **13**, 317 (1996)
78. M. Joffre: Measurement of spectral phase using spectrally-resolved upconversion, 1997, unpublished
79. V.G. Dmitriev, G.G. Gurzadyan, D.N. Nikogosyan: *Handbook of Nonlinear Optical Crystals*, (Springer, Berlin 1991), Chapter 2
80. P.N. Butcher, D. Cotter: *The Elements of Nonlinear Optics*, (Cambridge Univ.Press, Cambridge 1990) p. 220
81. J.E. Rothenberg, D. Grischkowsky: J. Opt. Soc. Am. B **2**, 626 (1985)
82. R.L. Fork, C.V. Shank, R. Yen, C.A. Hirlimann: IEEE J. Quantum Electron. **19**, 500 (1983)
83. G.P. Agrawal: *Nonlinear Fiber Optics* 2nd ed. (Academic Press, San Diego 1995)
84. E. Bourkoff, W. Zhao, R.I. Joseph, D.N. Christodoulides: Opt. Lett. **12**, 272 (1987)
85. E. Bourkoff, W. Zhao, R.I. Joseph, D.N. Christodoulides: Opt. Commun. **62**, 284 (1987)
86. W. Zhao, E. Bourkoff: IEEE J. Quantum Electron. **24**, 365 (1988)
87. W. Zhao, E. Bourkoff: Appl. Phys. Lett. **50**, 1304 (1987)
88. N. Kubota, M. Nakazawa: Opt. Commun. **66**, 79 (1988)
89. W. Rudolph, B. Wilhelmi: *Light Pulse Compression* (Harwood, 1989)
90. M.A. Duguay, J.W. Hansen: Appl. Phys. Lett. **14**, 14 (1969)
91. F. Gires, P. Tournois: C. R. Acad. Sci. Paris **258**, 6112 (1964)
92. W.J. Tomlinson, W.H. Knox: J. Opt. Soc. Am B **4**, 1404 (1987)
93. C.H. Brito Cruz, P.C. Becker, R.L. Fork, C.V. Shank: Opt. Lett. **13**, 123 (1988)
94. R. Szipöcs, K. Ferencz, Ch. Spielmann, F. Krausz: Opt. Lett. **19**, 201 (1994)
95. J.A. Britten, M.D. Perry, B.W. Shore, R.D. Boyd: Opt. Lett. **21**, 540 (1996)
96. Ch. Spielmann, M. Lenzner, F. Krausz, R. Szipöcs: Opt. Commun. **120**, 321 (1995)
97. M. Lenzner, Ch. Spielmann, E. Wintner, F. Krausz, A.J. Schmidt: Opt. Lett. **20**, 1397 (1995)
98. A.P. Kovacs, K. Osvay, Z. Bor, R. Szipöcs: Opt. Lett **20**, 788 (1995)
99. J. Kuhl, J. Heppner: IEEE J. Quantum Electron. **22**, 182 (1986)
100. K.D. Li, W.H. Knox, N.M. Pearson: Opt. Lett. **14**, 459 (1989)
101. R. Szipöcs, K. Ferencz, A. Mahig, F. Krausz, Ch. Spielmann: Proc. SPIE **1983**, 182 (1993)
102. B.E. Lemoff, C.P.J. Barty: Opt. Lett. **18**, 1651 (1993)
103. C. DeWitt Coleman, W.R. Bozman, W.F. Meggers: *Table of Wavenumbers* National Bureau of Standards Monograph 3, 1960
104. Melles-Griot: Optics Guide **5**, Chapt. 3
105. A.M. Weiner, J.P. Heritage, E.M. Kirschner: J. Opt. Soc. Am. B **5**, 1563 (1988)
106. A. Efimov, C. Schaffer, D.H. Reitze: J. Opt. Soc. Am. B **12**, 1968 (1995)
107. M.M. Wefers, K.A. Nelson: Opt. Lett. **18**, 2032 (1993)
108. J.-C. Diels, J.J. Fontaine, I.C. McMichael, F. Simoni: Appl. Opt. **24**, 1270 (1985)
109. W.P. de Boeij, M.S. Pshenichnikov, D.A. Wiersma: Chem. Phys. Lett. **238**, 1 (1995)
110. W.P. de Boeij, M.S. Pshenichnikov, D.A. Wiersma: Chem. Phys. Lett. **247**, 264 (1995)
111. Ch. Spielmann, F. Krausz: Appl. Optics **36**, 2523 (1997)
112. A. Stingl, M. Lenzner, Ch. Spielmann, F. Krausz, R. Szipöcs: Opt. Lett. **20**, 602 (1995)
113. B.E. Lemoff, C.P.J. Barty: Opt. Lett. **19**, 1367 (1992)
114. W.H. Press, S.A. Teukolsky, W.T. Vetterling, B.P. Flannery: *Numerical recipes in C: The Art of Scientific Computing* 2nd ed. (Cambridge University Press, Cambridge 1992), Chapt. 15
115. J.B. Peatross, T.D. Rockwood, G. Cook: Proceedings of OSA Annual Meeting /ILS-XII (Rochester, October 20–24, 1996), paper ThD3, p.163
116. J.B. Peatross, A. Rundquist: Temporal decorrelation of short laser pulses, submitted to J. Opt. Soc. Am. B (1997)
117. T. Andersson, S.T. Eng: Opt. Commun. **47**, 288 (1983)
118. C. Yan, J.-C. Diels: J. Opt. Soc. Am. B **8**, 1259 (1991)
119. K. Naganuma, K. Mogi, H. Yamada: Appl. Phys. Lett. **54**, 1201 (1989)
120. R.W. Gerchberg, W.O. Saxton: Optik **35**, 237 (1972)
121. A.M.J. Huiser, A.J.J. Drenth, H.A. Ferwerda: Optik **45**, 303 (1976)
122. A. Migus, Y. Gaudel, J.L. Martin, A. Antonetti: Phys. Rev. Lett. **58**, 1559 (1987)
123. F.H. Long, H. Lu, K.B. Eisenthal: Phys. Rev. Lett. **64**, 1469 (1990)
124. F.J. Webster, J. Schnitker, M.S. Friedrichs, R.A. Friesner, P.J. Rossky: Phys. Rev. Lett **66**, 3172 (1991)
125. T.H. Murphrey, P.J. Rossky: J. Chem. Phys. **99**, 515 (1993)
126. B.J. Schwartz, P.J. Rossky: J. Chem. Phys. **101**, 6902 (1994)
127. Y. Kimura, J.C. Alfano, P.K. Walhout, P.F. Barbara: J. Phys. Chem. **98**, 3450 (1994)
128. D.T. Reid, M. Padgett, C. McGowan, W.E. Sleat, W. Sibbett: Opt. Lett. **22**, 233 (1997)
129. W. Rudolph, M. Sheik Bahae, A. Bernstein, F. Lester: Opt. Lett. **22**, 313 (1997)
130. J.K. Ranka, A.L. Gaeta, A. Baltuška, M.S. Pshenichnikov, D.A. Wiersma, submitted to Opt. Lett., (1997)